Photoionization delays in xenon using single-shot referencing in the collinear back-focusing geometry

Author(s):
Jain, Arohi; Gaumnitz, Thomas; Bray, Alexander; Kheifets, Anatoli; Wörner, Hans Jakob

Publication date:
2018-09-15

Permanent link:
https://doi.org/10.3929/ethz-b-000293177

Originally published in:
Optics Letters 43(18), https://doi.org/10.1364/OL.43.004510

The following article appeared in Opt. Lett. 43, 4510 (2018) and may be found at https://doi.org/10.1364/OL.43.004510

Photoionization delays in xenon using single-shot referencing in the collinear back-focusing geometry

AROHI JAIN[1*], THOMAS GAUMNITZ[1], ALEXANDER BRAY[2], ANATOLI KHEIFETS[2], AND HANS JAKOB WÖRNER[1]

[1] *Laboratorium für Physikalische Chemie, ETH Zürich, Vladimir-Prelog-Weg 2, 8093 Zürich, Switzerland*
[2] *Research School of Physics and Engineering, The Australian National University, Canberra ACT 0200, Australia*
[*] *Corresponding author: Thomas.Gaumnitz@phys.chem.ethz.ch*

Compiled August 2, 2018

Attosecond photoemission delays for all the valence ($5p_{3/2}$, $5p_{1/2}$, 5s, $4d_{5/2}$, $4d_{3/2}$) subshells of xenon have been accessed using the interferometric RABBITT technique. The 4d subshell delays in Xe have been accessed for the first time due to the high photon energy used. A novel technique of single-shot referencing in the collinear back-focusing geometry has been introduced. This enables us to distinguish the signal from principal photoelectron peaks due to ionization by extreme ultraviolet radiation (XUV) only and infrared (IR) -induced sideband (SB) contributions, especially in the regions of spectral overlap.

OCIS codes: (020.0020) Atomic and Molecular Physics; (320.7100) Ultrafast measurements; (140.7240) UV, EUV, and X-ray lasers.

http://dx.doi.org/10.1364/XX.XX.XXXXXX

1. INTRODUCTION

An important feat of attosecond science in the recent years has been its application in accessing the photoemission time delay in atoms [1–3], solids [4–6] and molecules [7, 8]. With the recent developments, attosecond chronoscopy has become a major area of research within attosecond science since its first application by Cavalieri *et al.*[4]. The advances in ultrashort pulse generation [9] and characterization [10] further opens opportunities to follow the temporal evolution in a more precise manner.

So far spin-orbit photoemission time delays [11] have largely remained unaccessed, with Jordan *et al.*[11] demonstrating the first experimental application in krypton and xenon. Recently, Isinger *et al.*[12] accessed photoemission delays in neon at high XUV photon energies using the interferometric reconstruction of attosecond beating by two photon transitions (RABBITT) technique [13], and compared it with photoemission time delays obtained from attosecond streaking by Schultze *et al.*[1]. To access photoemission delays between spin-orbit states, an implementation of RABBITT technique is indispensable due to the required energy resolution.

In this article, we present experimental techniques and results, where we access for the first time spin-orbit photoemission time delays in xenon, particularly for 4d subshell. These have been theoretically discussed recently [14] in the framework of xenon confinement in carbon fullerenes.

The usage of a chopper wheel in a forward-focusing active interferometric setup has been shown in [7, 11] to access spin-orbit delays in noble gas atoms. However, 4d photoemission delays have not been measured until now, as they require higher XUV photon energies ($E_{\mathrm{phot}} > 68\,\mathrm{eV}$). At such high energies, a long harmonic comb is formed, where filtering with metallic foils still results in several harmonic orders that may overlap in the photoelectron spectrum. Furthermore, the spectral overlap due to Auger emission lines also adds to the unresolved contributions.

To enhance the modulation depth of the sideband oscillations, shot-to-shot pump (XUV) and pump-probe (XUV+IR) referencing is an optimal solution and will be discussed in this paper. A custom-made chopper wheel is therefore introduced into the beam path for this purpose. This is a novel implementation in the case of a back-focusing geometry since a standard chopper for a co-propagating XUV-IR geometry would block both, XUV and IR, beams. A special chopper setup blocks only every other shot of the IR beam at half the repetition rate of the laser and therefore allows for single-shot referencing. Here we demonstrate the combination of both above mentioned advancements in technology with complex photoelectron spectra of xenon including spin-orbit splitting. This new technique will also be applicable to attosecond interferometry of complex gaseous and liquid systems.

Section 2 contains the description of the experimental setup. In Section 3, we present our experimental results, where we exemplify RABBITT with the chopper and show the comparison with theory. Conclusions and outlook are presented in Section 4.

2. EXPERIMENTAL SETUP

The experimental setup is shown in Fig. 1 and is described in detail in [15]. 25-fs long, 700 μJ pulses from a 1 kHz Ti:Sapphire laser system (Femtolasers Femtopower pro V) are focused to a high-harmonic helium gas target with a silver focusing mirror (f=50 cm). A typical harmonic spectrum is shown in Fig. 1 as an inset. Modifications to the generation conditions, such as changes to the gas pressure, target position or peak intensity, can shift the harmonic spectra across the mirror reflectivity curve.

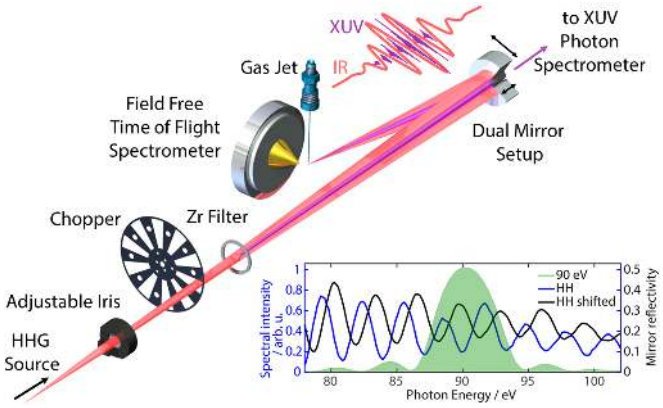

Fig. 1. Attosecond pump-probe beamline in backward focusing geometry. The generated harmonics from high harmonic generation (HHG) source co-propagate collinearly with the residual IR beam. A zirconium metal foil spectrally filters the HHG in the center and the IR beam intensity is controlled by a motorized iris. A special chopper wheel allows for single-shot referencing by allowing IR beam transmission only at every second shot. The beams are focused using a dual mirror assembly on a gas jet and the generated photoelectrons are detected using a field-free time-of-flight spectrometer. Mirror reflectivity curve (green), overlaid with high harmonic spectra with different generation conditions, allowing control of reflectivity of one or two harmonics is shown in the inset.

After high-order harmonic generation, both the residual IR and the generated XUV beams collinearly co-propagate together. A motorized iris controls the intensity of the IR beam for the RABBITT experiments. This plays an important role as excess of IR intensity can lead to multi-photon RABBITT [16] and increase the complexity of the data analysis. It is important to note that since the XUV has a smaller divergence as compared to the IR, only the IR intensity is controlled using the iris during the measurement. A thin metallic foil, matching the beam diameter of the XUV is introduced into the beam bath, such that the residual IR in the XUV beam path is suppressed.

A custom made chopper blade mounted on an optical chopper system (Thorlabs MC2000) synchronized with the laser pulses, is introduced into the beam path for single-shot referencing of XUV (closed) vs XUV+IR (open) experiments, shown in Fig. 1. It is to be noted that the implementation of our chopper wheel is different compared to those that have been reported till now. Since the XUV and IR beams are co-propagating, and there are no separate pathways for the beams [17], the chopper has to be prepared such that the XUV stays unaffected, while the IR signal is alternated between consecutive shots. The IR is therefore filtered out at half the repetition rate of the laser. Such fast mechanical movements are not allowed by the iris assembly. The custom chopper assembly further improves the signal to noise ratio. Long term XUV intensity instabilities can be compensated by referencing shot-to-shot. The diameter of the hole matches with that of the filter, such that only the XUV propagates for one shot, and in the next one the whole beam passes through. The advantage of introducing the chopper, for this back-focusing geometry is described later.

The flux of the high-order harmonics is optimized using a home-made XUV photon spectrometer described elsewhere [15]. The iris is centered for the maximum flux of the XUV source, and filter and chopper wheel are also positioned to allow only the XUV through the closed position of the chopper. A dual mirror assembly [18] is used to refocus the co-propagating XUV and IR beams onto a xenon gas target. The inner mirror is a multi-layer mirror optimized for reflectivity at $E_{\mathrm{phot}} = 90\,\mathrm{eV}$ with a bandwidth of $\Delta E = 5\,\mathrm{eV}$ (cf. Fig. 1 inset). It is mounted on a piezo-linear stage to set the delay between XUV- and IR-pulse. The outer mirror reflects the IR beam. An imaging mirror after the interaction region redirects the beam onto a camera and is used to determine the position of spatial and temporal overlap.

3. EXPERIMENTAL RESULTS

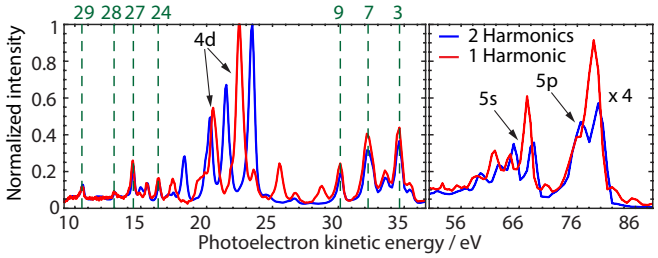

Fig. 2. Photoelectron spectra measured in xenon by shifting the HHG spectrum with respect to the reflective bandwidth of the multi-layer mirror. Xenon $N_{4,5}OO$ Auger peaks (green) are marked with dashed lines (Auger-electron lines are labeled according to [19, 20].), and do not change their positions when changing the input photon energy. The photoemission lines from the 5p, 5s and 4d subshells shift in position and number according to reflected high-harmonic spectrum. The spectrum in the kinetic energy range of 54-90 eV is amplified by 4 for better visibility. The difference in intensity comes from the different cross sections of 5p, 5s and 4d at $E_{\mathrm{phot}} = 90\,\mathrm{eV}$.

A. Static photoelectron spectra

Auger electrons emitted from the photoionization of xenon [19, 20] using high-order harmonics are used to calibrate the field-free time-of-flight spectrometer [21]. A field-free photoelectron spectrum obtained with xenon is shown in Fig. 2. The multi-layer mirror centered at 90 eV reflects the harmonic orders 57 and 59, shown in Fig. 1, while the other harmonics are suppressed. Using the multi-layer mirror gives us control over the number of harmonic orders used in the experiment. Restricting them to two for the present case proves to be an advantage as this leads to minimal spectral overlap, hence cleaner traces and simpler data analysis. We can reference the sideband oscillations directly for the interesting photoemission lines to obtain the relative delays. HHG can be tuned/blue-shifted by changing the pulse compression or gas pressure to optimize for the case when the peak of one harmonic overlaps with the maximum of the mirror reflectivity. The photoelectron spectra recorded from a single harmonic line can be used to determine the principal-component photoelectron spectra and to extract the information on energy-dependent cross sections for the target species. This technique can be used for complex species, such as liquid water. The obtained photoelectron spectrum for the case of two harmonics compared to a single harmonic for xenon is shown in Fig. 2 using a deceleration of $U_{\mathrm{ret}} = 5\,\mathrm{V}$ to remove the low-energy background and a coil current of $I_{\mathrm{coil}} = 0.3\,\mathrm{A}$ to increase the collection efficiency. The positions of the Auger electrons remain unaffected from the change in the XUV spectrum.

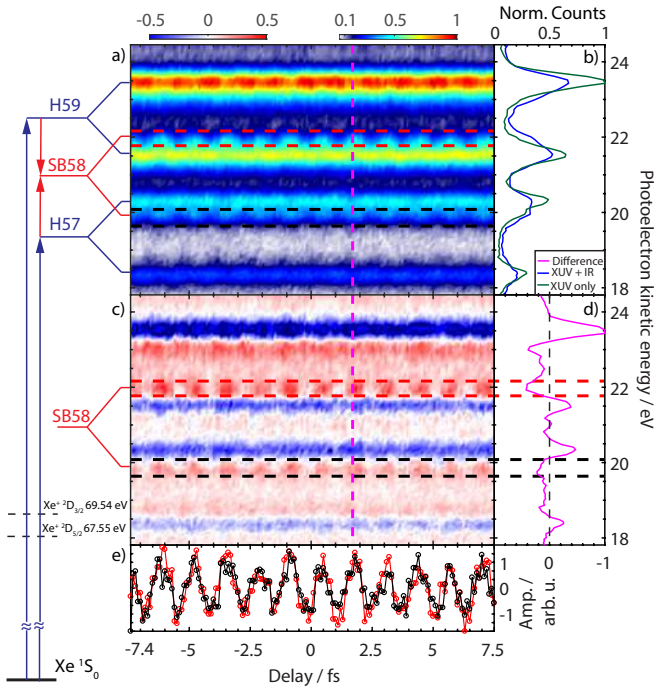

Fig. 3. XUV+IR RABBITT interferogram (a) and difference (XUV+IR - XUV-only) interferogram (c) measured in Xe with attosecond pulse train consisting of H57 and H59 and IR pulse centered at 800 nm. A cross-cut of the photoelectron spectra corresponding to the dashed magenta line is shown in (b) and (d). The oscillating sideband (e) is obtained by averaging the sideband signal for $4d_{5/2}$ (black) and $4d_{3/2}$ (red).

B. RABBITT

With a central IR wavelength of $\lambda_L = 800$ nm, the odd harmonics are separated by $2E_L = 3.1$ eV, and the sideband lies at an interval of 1.55 eV from the harmonics. For xenon, the spin-orbit interaction leads to splitting of the ionization thresholds with $4d_{5/2}$ (IP=67.55 eV) and $4d_{3/2}$ (IP=69.54 eV) [22–24] and in 5p with $5p_{3/2}$ (IP=12.13 eV) and $5p_{1/2}$ (IP=13.44 eV) [11, 25]. For a harmonic order n, the $4d_{3/2}$ (or $5p_{1/2}$) photoelectron peak is then very close to the SB (n+1) associated with the $4d_{5/2}$ (or $5p_{3/2}$) vacancy. This leads to a partial overlap and hence decreases the modulation depth of the time dependent two-photon photoionization signal. To resolve this issue, a special custom-made chopper for collinear beam geometry of IR/XUV is implemented, as described in Section 3. The chopper wheel blocks only the IR beam for every other laser shot. Therefore, the XUV-only spectra can be recorded in alternation with two-color (XUV+IR) spectra. Time-resolved photoelectron spectra as a function of XUV-IR delay are shown without chopper for 4d splitting in Fig. 3(a,b) and with chopper after referencing to the XUV only signal is shown in Fig. 3(c,d). A deceleration of only $U_{ret} = 5$ V is applied for the case of 4d electrons. A deceleration of $U_{ret} = 50$ V is applied to increase the resolution of the recorded time-resolved interferogram for the outer valence orbitals, i.e., $5p_{3/2}$, $5p_{1/2}$ and 5s. The displayed spectrum is therefore shifted by 5 eV kinetic energy and matches well with the expected ionization potential. In both cases, a coil current [21] of $I_{coil} = 0.3$ A is applied to enhance the collection efficiency. Panels (b) and (d) show the photoelectron spectra measured at the delay position marked with a dashed magenta line in panels (a) and (c). The XUV-only photoelectron spectra have clearly higher intensity in the principal photoelectron peaks from the harmonics compared to the XUV+IR spectra. In the XUV+IR spectra, the contribution in the sideband photoelectron spectra results in the loss of intensity in the harmonic photoelectron peaks. For clear visualization of the RABBITT oscillations, the integrated sideband region is shown in panel (e). Recently, Jordan *et al.*[26] developed a technique to extract delay information from spectrally overlapping spectrograms. In this article, we apply this technique to obtain the phases from the spectrally overlapping $4d_{3/2}$ sideband with $4d_{5/2}$ harmonic peak. We start with the XUV only photoelectron spectra, where no sideband peaks are present. Fitting of the principal peaks from H57 and H59 of $4d_{3/2}$ and $4d_{5/2}$, provide us with the values for the intensity and width of these peaks. Using this information, the fit of delay-integrated XUV+IR interferogram gives additional information on the sideband intensity, width and position. The intensity, width and peak positions are finally optimized by fitting the delay-integrated difference spectra. A complex-valued fit parameter z_j is then assigned to each photoelectron band, including the principal peaks and the sidebands, obtained from fitting the delay integrated difference spectra. A time-resolved difference spectrogram is Fourier transformed along the time axis. An integration is performed within user-defined boundaries around the $2\omega_L$ oscillation peak, which results in a one-dimensional complex array along the photoelectron kinetic energy axis, denoted as $I(E)$. This complex array $I(E)$ obtained from the measured trace is then fitted using the information on photoelectron bands, and the complex numbers assigned to each band are used as fit parameters. The imaginary part $\Delta\phi$ of z_j gives the phase of the associated photoelectron band. The relative delay between the two bands can then be calculated as follows:

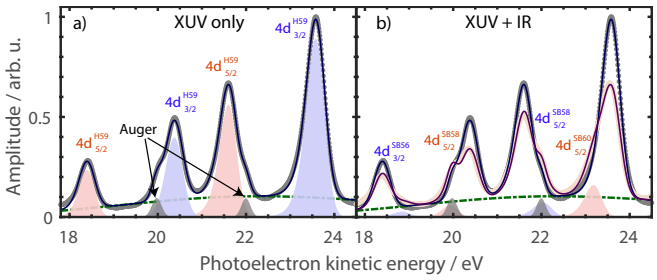

Fig. 4. (a) Principal-component fit for XUV-only photoelectron spectra, marked by contributions from H57 and H59 of $4d_{5/2}$ and $4d_{3/2}$, which partially overlap with xenon $N_{4,5}OO$ Auger peak number 16 and 18 (labels according to [19, 20]). (b) Modeling of XUV+IR photoelectron spectra, including sideband contributions and decrease in principal XUV peak intensity.

$$\tau(\mathrm{Xe}_{4d_{5/2}}) - \tau(\mathrm{Xe}_{4d_{3/2}}) = \frac{1}{2\omega_L}\left[\Delta\phi(\mathrm{Xe}_{4d_{5/2}}) - \Delta\phi(\mathrm{Xe}_{4d_{3/2}})\right] \quad (1)$$

$\Delta\phi$ contains contributions from spectral phase of the harmonic orders and the atomic phase of the photoelectron wavepacket. The atomic part includes the Wigner time-delay τ_{EWS} due to photoionization by XUV radiation and the continuum-continuum delay τ_{CC} which arises from the subsequent absorption of an IR photon in the presence of the Coulomb potential. Similar analysis has been performed for obtaining the delays between $5p_{3/2}$, $5p_{1/2}$ and 5s. Since the sidebands for different orbitals are formed with the same harmonic orders, the contribution

Table 1. Measured delays τ_{meas} versus calculated difference $\tau_{calc} = \tau_{EWS_1} + \tau_{CC_1} - \tau_{EWS_2} - \tau_{CC_2}$ of the Wigner [27] time delays τ_{EWS} [14, 25, 28] and continuum-continuum corrections τ_{CC} [25, 29] in Xe for $E_{phot} = 90$ eV. All τ are in attoseconds.

$orb_1 - orb_2$	τ_{meas}	τ_{EWS_1}	τ_{CC_1}	τ_{EWS_2}	τ_{CC_2}	τ_{calc}
$4d_{5/2}$-$4d_{3/2}$	-4.0 ± 4.1	57.5	−28.7	64.3	−31.8	−3.7
5p - 5s	$+3.6 \pm 5.3$	18.5	−6.7	17.2	−8.0	+2.6
$5p_{3/2}$-$5p_{1/2}$	$+14.5 \pm 9.3$	18.8	−6.6	19.5	−6.7	−0.6

to phase from the difference in spectral phases of the involved harmonic cancels out, allowing for the extraction of the phase difference of $5p_{3/2}$-5s and $4d_{5/2}$ and $4d_{3/2}$. Combining the single-shot referencing with a multi-layer mirror that reflects only two harmonic orders allows therefore to systematically extract the energy dependent delays with high fidelity and high signal-to-noise ratio. The delays between photoelectron wavepackets emitted from the $5p_{3/2}$, $5p_{1/2}$, 5s, $4d_{5/2}$ and $4d_{3/2}$ subshells of Xe, as extracted from the fit results, are shown in Table 1. The measured delay between the $4d_{5/2}$ and $4d_{3/2}$ photoelectrons of -4.0 ± 4.1 as from 22 measurements is in close agreement with the calculated difference of the Wigner delay augmented by the continuum-continuum correction, yielding a calculated delay of -3.7 as. Direct RABBITT simulation by solving the time-dependent Schrödinger equation as in [30] gives a $4d_{5/2}$-$4d_{3/2}$ time delay difference of -15 as. The calculated 5p-5s delay also agrees with the measured value (average over 19 measurements). The $5p_{3/2}$-$5p_{1/2}$ delay, however, does not agree with the measurement, as the measured delay of 14.5 ± 9.3 as (17 measurements) is significantly larger than the calculated delay of -0.6 as. A similar discrepancy has been observed at much lower photon energies by Jordan *et al.* [11]. This was attributed to the presence of resonances of doubly-excited character which were also reported for high energies by Chen *et al.* [31].

4. SUMMARY AND OUTLOOK

In this article, we have demonstrated a single-shot referencing technique for the co-propagating IR and XUV beams in back-focusing geometry. This technique enables attosecond measurements with high signal to noise ratio, specially relevant for spectrally overlapping photoelectron bands and small signal changes. We have also shown that spin-orbit photoemission delays in Xe can be measured with this technique, including the 4d subshell which was so-far not accessed in attosecond time-resolved measurements. This technique finds applications in all co-propagating pump-probe beams, where an XUV signal is required to distinguish the underlying features that have either been lost in the background from XUV-IR or the photoelectron bands have shifted in presence of IR, and the initial position of the bands is crucial for analysis and data interpretation.

A.J. and T.G. contributed equally to this work. We thank Andrés Laso, Andreas Schneider and Michael Fiechter from our electronic and mechanical workshop at ETH/D-CHAB for their excellent support.
Funding Information: ERC Starting Grant (contract 307270-ATTOSCOPE); ETH Zürich; SNF (200021E_162822).

REFERENCES

1. M. Schultze, M. Fieß, N. Karpowicz, J. Gagnon, M. Korbman, M. Hofstetter, S. Neppl, A. L. Cavalieri, Y. Komninos, T. Mercouris, C. A. Nicolaides, R. Pazourek, S. Nagele, J. Feist, J. Burgdörfer, A. M. Azzeer, R. Ernstorfer, R. Kienberger, U. Kleineberg, E. Goulielmakis, F. Krausz, and V. S. Yakovlev, Science **328**, 1658 (2010).
2. K. Klünder, J. M. Dahlström, M. Gisselbrecht, T. Fordell, M. Swoboda, D. Guénot, P. Johnsson, J. Caillat, J. Mauritsson, A. Maquet, R. Taïeb, and A. L'Huillier, Phys. Rev. Lett. **106**, 143002 (2011).
3. C. Cirelli, C. Marante, S. Heuser, C. L. M. Petersson, Á. J. Galán, L. Argenti, S. Zhong, D. Busto, M. Isinger, S. Nandi, S. Maclot, L. Rading, P. Johnsson, M. Gisselbrecht, M. Lucchini, L. Gallmann, J. M. Dahlström, E. Lindroth, A. L'Huillier, F. Martín, and U. Keller, Nat. Commun. **9**, 955 (2018).
4. A. L. Cavalieri, N. Müller, T. Uphues, V. S. Yakovlev, A. Baltuška, B. Horvath, B. Schmidt, L. Blümel, R. Holzwarth, S. Hendel, M. Drescher, U. Kleineberg, P. M. Echenique, R. Kienberger, F. Krausz, and U. Heinzmann, Nature. **449**, 1029 (2007).
5. R. Locher, L. Castiglioni, M. Lucchini, M. Greif, L. Gallmann, J. Osterwalder, M. Hengsberger, and U. Keller, Optica. **2**, 405 (2015).
6. S. Neppl, R. Ernstorfer, A. L. Cavalieri, C. Lemell, G. Wachter, E. Magerl, E. M. Bothschafter, M. Jobst, M. Hofstetter, U. Kleineberg, J. V. Barth, D. Menzel, J. Burgdörfer, P. Feulner, F. Krausz, and R. Kienberger, Nature. **517**, 342 (2015).
7. M. Huppert, I. Jordan, D. Baykusheva, A. von Conta, and H. J. Wörner, Phys. Rev. Lett. **117**, 093001 (2016).
8. V. V. Serov and A. S. Kheifets, J. Chem. Phys. **147**, 204303 (2017).
9. T. Gaumnitz, A. Jain, Y. Pertot, M. Huppert, I. Jordan, F. Ardana-Lamas, and H. J. Wörner, Opt. Express **25**, 27506 (2017).
10. T. Gaumnitz, A. Jain, and H. J. Wörner, Opt. Express **26**, 14719 (2018).
11. I. Jordan, M. Huppert, S. Pabst, A. S. Kheifets, D. Baykusheva, and H. J. Wörner, Phys. Rev. A **95**, 013404 (2017).
12. M. Isinger, R. J. Squibb, D. Busto, S. Zhong, A. Harth, D. Kroon, S. Nandi, C. L. Arnold, M. Miranda, J. M. Dahlström, E. Lindroth, R. Feifel, M. Gisselbrecht, and A. L'Huillier, Science **358**, 893 (2017).
13. P. M. Paul, E. S. Toma, P. Breger, G. Mullot, F. Augé, P. Balcou, H. G. Muller, and P. Agostini, Science **292**, 1689 (2001).
14. A. Mandal, P. C. Deshmukh, A. S. Kheifets, V. K. Dolmatov, and S. T. Manson, Phys. Rev. A **96**, 053407 (2017).
15. A. Jain, T. Gaumnitz, and H. J. Wörner, publication –, (2018).
16. M. Swoboda, J. M. Dahlström, T. Ruchon, P. Johnsson, J. Mauritsson, A. L'Huillier, and K. J. Schafer, Laser Phys. **19**, 1591 (2009).
17. M. Huppert, I. Jordan, and H. J. Wörner, Rev. Sci. Instrum. **86**, 123106 (2015).
18. M. Schultze, A. Wirth, I. Grguras, M. Uiberacker, T. Uphues, A. Verhoef, J. Gagnon, M. Hofstetter, U. Kleineberg, E. Goulielmakis, and F. Krausz, J. Electron Spectrosc. Relat. Phenom. **184**, 68 (2011).
19. L. O. Werme, T. Bergmark, and K. Siegbahn, Phys. Scr. **6**, 141 (1972).
20. T. Carroll, J. Bozek, E. Kukk, V. Myrseth, L. Sæthre, T. Thomas, and K. Wiesner, J. Electron. Spectrosc. Relat. Phenom. **125**, 127 (2002).
21. I. Jordan, A. Jain, T. Gaumnitz, J. Ma, and H. J. Wörner, Rev. Sci. Instrum. **89** (2018).
22. G. C. King, M. Tronc, F. H. Read, and R. C. Bradford, J. Phys. B **10**, 2479 (1977).
23. K. Codling and R. Madden, Phys. Rev. Lett. **12**, 106 (1964).
24. S. Shannon, K. Codling, and J. West, J. Phys. B **10**, 825 (1977).
25. A. Kheifets, Phys. Rev. A **87**, 063404 (2013).
26. I. Jordan and H. J. Wörner, J. Opt. **20**, 024013 (2018).
27. E. P. Wigner, Phys. Rev. **98**, 145 (1955).
28. A. Kheifets, A. Mandal, P. C. Deshmukh, V. K. Dolmatov, D. A. Keating, and S. T. Manson, Phys. Rev. A **94**, 013423 (2016).
29. J. Dahlström, A. L'Huillier, and A. Maquet, J. Phys. B **45**, 183001 (2012).
30. A. W. Bray, F. Naseem, and A. S. Kheifets, Phys. Rev. A **97**, 063404 (2018).
31. Y.-J. Chen, S. Pabst, and R. Santra, J. Phys. Commun. **2**, 045024 (2018).